

An elasto-viscoplastic constitutive model for the rate-dependent behavior of polyvinylidene fluoride

Citation for published version (APA):

Lenders, T., Remmers, J. J. C., Pini, T., Veenstra, P., Govaert, L. E., & Geers, M. G. D. (2023). An elasto-viscoplastic constitutive model for the rate-dependent behavior of polyvinylidene fluoride. *Journal of Polymer Science*, 61(14), 1439-1456. <https://doi.org/10.1002/pol.20220729>

DOI:

[10.1002/pol.20220729](https://doi.org/10.1002/pol.20220729)

Document status and date:

Published: 15/07/2023

Document Version:

Publisher's PDF, also known as Version of Record (includes final page, issue and volume numbers)

Please check the document version of this publication:

- A submitted manuscript is the version of the article upon submission and before peer-review. There can be important differences between the submitted version and the official published version of record. People interested in the research are advised to contact the author for the final version of the publication, or visit the DOI to the publisher's website.
- The final author version and the galley proof are versions of the publication after peer review.
- The final published version features the final layout of the paper including the volume, issue and page numbers.

[Link to publication](#)

General rights

Copyright and moral rights for the publications made accessible in the public portal are retained by the authors and/or other copyright owners and it is a condition of accessing publications that users recognise and abide by the legal requirements associated with these rights.

- Users may download and print one copy of any publication from the public portal for the purpose of private study or research.
- You may not further distribute the material or use it for any profit-making activity or commercial gain
- You may freely distribute the URL identifying the publication in the public portal.

If the publication is distributed under the terms of Article 25fa of the Dutch Copyright Act, indicated by the "Taverne" license above, please follow below link for the End User Agreement:

www.tue.nl/taverne

Take down policy

If you believe that this document breaches copyright please contact us at:

openaccess@tue.nl

providing details and we will investigate your claim.

RESEARCH ARTICLE

An elasto-viscoplastic constitutive model for the rate-dependent behavior of polyvinylidene fluoride

Tom Lenders¹  | Joris J. C. Remmers¹  | Tommaso Pini¹  |
Peter Veenstra² | Leon E. Govaert¹  | Marc G. D. Geers¹ 

¹Department of Mechanical Engineering,
Eindhoven University of Technology,
Eindhoven, the Netherlands

²Shell Global Solutions International B.V.,
Amsterdam, the Netherlands

Correspondence

Joris J. C. Remmers, Department of
Mechanical Engineering, Eindhoven
University of Technology, Eindhoven
5600MB, the Netherlands.
Email: j.j.c.remmers@tue.nl

Funding information

Shell Global Solutions International B.V.

Abstract

To model the engineering performance of components made of polyvinylidene fluoride (PVDF), the 3D elasto-viscoplastic Eindhoven glassy polymer (EGP) model is extended to describe the rate-dependent behavior of PVDF. Careful analysis of the intrinsic behavior of PVDF revealed that the postyield compressive response shows a strain rate-dependence that evolves with increasing deformation. The extension of the constitutive model captures the deformation-dependent evolution of the activation volume and the rate-factor, which describes the driving stress. Given the significant temperature-dependent behavior, the model has been characterized for different temperatures (23, 55 and 75 °C). The accuracy of the model has been validated by means of tension and creep experiments at these temperatures. The constitutive model is implemented in finite element simulations and the results are compared with the experiments. It is shown that the proposed model allows for an accurate prediction of the short- and long-term rate-dependent behavior of PVDF.

KEYWORDS

EGP-model, elasto-viscoplastic material, finite element simulations, polyvinylidene fluoride

1 | INTRODUCTION

The increasing depth of offshore oil- and gas-fields at the seabed results in increasingly severe conditions to which structures in the offshore industry are exposed, for example, large temperature gradients, high pressures and chemically aggressive hydrocarbons. As a consequence, conventional steel pipelines used to transport water and hydrocarbons between seabed and platforms at sea-level, are being replaced by thermoplastic composite pipes (TCP). TCP are flexible multilayered systems composed of a thermoplastic fiber reinforced composite layer concealed by an inner liner and a

protective coating on the outside. The pipes are typically designed to allow for a maximum bending strain between 1.5% and 3.5%, depending on the application of the pipe. The bending strains are in the axial direction of the pipes and are therefore different from the strains in the unidirectional composite layers that depend on the fiber orientation with respect to the axial direction of the pipe. Furthermore, depending on the application of the TCP, the external pressure can increase to 350 bar while the internal pressure may vary between vacuum and 800 bar. The high mechanical strength, relatively lightweight nature and especially the chemical resistance to water and hydrocarbons

This is an open access article under the terms of the [Creative Commons Attribution](https://creativecommons.org/licenses/by/4.0/) License, which permits use, distribution and reproduction in any medium, provided the original work is properly cited.

© 2023 The Authors. *Journal of Polymer Science* published by Wiley Periodicals LLC.

make these pipes an excellent material for exploitation in offshore applications.

Polyvinylidene fluoride (PVDF) is the preferred matrix material in the fiber reinforced composite layer because of its high chemical resistance in combination with good mechanical and thermal properties. PVDF is a semicrystalline thermoplastic polymer that generally consists of two distinct crystalline phases, denoted as the α - and β -phase, respectively. The β -phase is associated with piezo- and pyroelectric properties, that is the ability to generate an electric charge when subjected to a mechanical or thermal load, respectively.¹ The α -phase is known for its strong mechanical performance and chemical resistance, which makes it suitable for applications in the offshore oil- and gas-industry.^{2,3}

In the past decades, most studies were focused on the piezoelectric properties of PVDF^{4–6} and the thermomechanical performance of α -phase PVDF received only little attention. To ensure a safe and reliable use of PVDF in oil- and gas-applications, its thermomechanical behavior should be well understood. In order to characterize the thermomechanical behavior of PVDF, numerical models can be of assistance. Numerical studies supplement experimental campaigns unraveling some observed phenomena. Yet, these models also reduce the amount of time- and resource demanding experimental efforts and they are instrumental for the engineering design of the components to be made.

The focus on the analysis of the constitutive behavior of PVDF and correspondingly, the development of numerical models is relatively limited. Reis et al.⁷ proposed a 1D elasto-viscoplastic model to describe the rate-dependent tensile response of PVDF at room temperature. Motta et al.⁸ introduced a 1D elasto-viscoplastic constitutive model to describe both cyclic and monotonic tensile loading at room temperature with both isotropic and kinematic hardening incorporated. Although strain hardening is included in the model, it is only applied to describe the behavior up to relatively small strains of 3%. Furthermore, both models assume that the entire nonlinear response is accounted for in the irreversible plastic part, whereas the deviation from the elastic response is not completely irreversible.

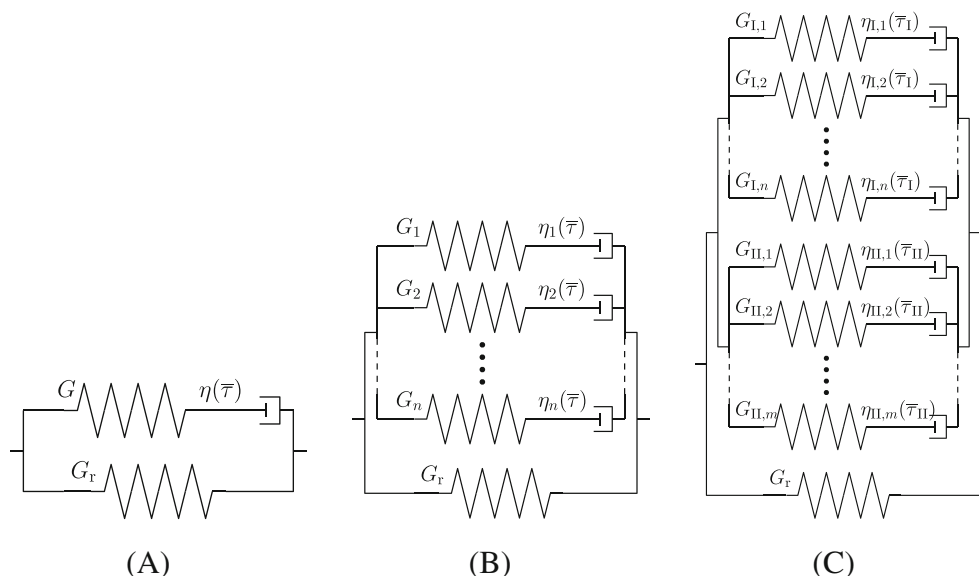
Challier et al.⁹ focused on the tensile response of PVDF at room temperature. They observed voiding and stress-whitening in tensile specimens and used a 3D elasto-viscoplastic modified Gurson model to describe the mechanical behavior. Laiarinandrasana et al.¹⁰ continued on this work and applied the modified Gurson model to describe the tensile response of PVDF at lower temperatures (down to -50 °C). This model is able to describe the tensile response of PVDF at moderate strain rates and low temperatures. Both models however, describe the

response up to the yield stress as linear elastic, resulting in a loss of information in the nonlinear preyield response of the material. O'Connor et al.¹¹ used a 3D viscoplastic constitutive model to describe the response of PVDF in microindentation tests, where they also adopted linear elastic behavior up to the yield point. Furthermore, the onset of plastic deformation is based on the Von-Mises yield criterion, which means that no pressure sensitivity is taken into account. Yet, the yield stress of polymer materials is well known to be pressure-dependent.

For the description of the intrinsic behavior of PVDF in a finite element setting, a 3D constitutive model is required that accurately describes the elasto-viscoplastic response up to large strains, at different strain rates and temperatures. In this work we present a fully 3D strain rate-dependent model based on the mechanical behavior of PVDF. The constitutive model described by van Breemen et al.,¹² referred to as Eindhoven glassy polymer (EGP)-model, is used as a starting point. In a recent experimental investigation of the yield kinetics of PVDF, Pini et al.¹³ showed that the yield response in compression and tension can be represented by a modified Ree-Eyring equation. Based on this study, we describe the time- and temperature-dependent behavior of PVDF using the 3D elasto-viscoplastic constitutive model by van Breemen et al.,¹² based on the Eyring flow theory.¹⁴ The model uses an Eyring flow viscosity which reduces with the applied stress, effectively reducing the relaxation time. A major benefit of this model is the incorporation of multiple relaxation times which enables an accurate description of the nonlinear response in the preyield regime. Furthermore, the flow viscosity is pressure dependent, making it suitable for complex loading conditions. The model has been successfully applied to describe the intrinsic rate- and temperature-dependent response of both amorphous and semicrystalline polymers requiring only a limited number of short-term experiments.^{12,15–17} The fact that the model is also capable of predicting the long-term response, using merely short-term experiments, makes it very powerful for engineering purposes.

To enable the large-strain description of the material, the model implementation is extended to describe the evolution of the strain rate-dependence with increasing deformation. The extension is based on the work of Wendlandt et al.¹⁸ and Senden et al.¹⁹ Wendlandt proposed a deformation-dependent activation volume to model the large-strain response of five different polymers and Senden proposed a deformation-dependence of either a rate-factor or the activation volume. A similar approach is proposed here, where a deformation-dependent activation volume and rate-factor are combined. Experiments on PVDF samples are used to identify the required

FIGURE 1 Mechanical analogs of the EGP-model: (A) single-mode model, (B) the multi-mode model and (C) the multi-process multi-mode model.



material parameters. Finally, the identified material parameters are used to validate the model by comparing finite element simulations of uniaxial tensile tests and tensile creep tests to experimental results.

This article is organized as follows. In Section 2 the constitutive model as described by van Breemen et al.¹² is briefly reviewed. This is followed by the experimental methods and corresponding test results on PVDF in Section 3. In Section 4 details of the finite element simulations are explained, after which in Section 5 the identification of the material parameters required for the constitutive model is discussed. This includes the proposed extension of the constitutive model. Subsequently, the extended constitutive model is validated in Section 6 and finally the conclusions are given in Section 7.

Throughout this article, scalar variables are denoted as a or A and second-order tensors are denoted as \mathbf{A} .

2 | CONSTITUTIVE MODEL

The 3D isotropic elasto-viscoplastic constitutive model described by van Breemen et al.¹² is used as a basis to describe the material behavior of PVDF. The key ingredients of this model are reviewed here. The proposed extension to this model is introduced later in Section 5.1.2.

The deformation gradient \mathbf{F} is multiplicatively decomposed into the elastic part \mathbf{F}_e and the plastic part \mathbf{F}_p as

$$\mathbf{F} = \mathbf{F}_e \cdot \mathbf{F}_p. \quad (1)$$

This means that the velocity gradient tensor \mathbf{L} is defined by an additive split of the elastic part \mathbf{L}_e and the plastic part \mathbf{L}_p as

$$\mathbf{L} = \dot{\mathbf{F}} \cdot \mathbf{F}^{-1} = \mathbf{L}_e + \mathbf{L}_p. \quad (2)$$

The rotation corresponding to the elastic and plastic part of the deformation is not uniquely defined by Equation (1). Therefore, it is assumed that the plastic deformation is spin-free which implies that

$$\mathbf{L}_p = \mathbf{D}_p + \mathbf{\Omega}_p = \mathbf{D}_p, \quad (3)$$

where \mathbf{D}_p is the plastic rate of deformation tensor and $\mathbf{\Omega}_p$ is the plastic spin tensor. In addition, the plastic deformation is assumed to be isochoric and therefore the volume change ratio J is defined as

$$J = \det(\mathbf{F}) = \det(\mathbf{F}_e). \quad (4)$$

The total stress $\boldsymbol{\sigma}$ is decomposed using an additive split of the driving stress $\boldsymbol{\sigma}_s$ and the hardening stress $\boldsymbol{\sigma}_r$:

$$\boldsymbol{\sigma} = \boldsymbol{\sigma}_s + \boldsymbol{\sigma}_r. \quad (5)$$

The mechanical representation of the model in its most simple form, that is the single-mode model, is shown in Figure 1A.²⁰ The driving stress represents the intermolecular interactions and is modeled using a single nonlinear Maxwell element. The hardening stress represents the elastic contribution of the entanglement network and is modeled by a single spring. For an accurate description of the nonlinear strain hardening, the Edward–Vilgis hardening model as introduced by Senden et al.¹⁶ is used. The hardening stress is formulated as

$$\boldsymbol{\sigma}_r = \frac{G_r}{J} (\tilde{\mathbf{B}} \cdot \mathbf{Z})^d, \quad (6)$$

where G_r is the hardening modulus, $\tilde{\mathbf{B}}$ the isochoric left Cauchy–Green strain tensor. The second-order tensor \mathbf{Z} is defined as

$$\begin{aligned} \mathbf{Z} = & \frac{\alpha_r^2(1+\xi_r)(1-\alpha_r^2)}{(1-\alpha_r^2\text{tr}(\tilde{\mathbf{B}}))^2} \text{tr} \left(\tilde{\mathbf{B}} \cdot \left(\mathbf{I} + \xi_r \tilde{\mathbf{B}} \right)^{-1} \right) \mathbf{I} \\ & + \frac{(1+\xi_r)(1-\alpha_r^2)}{1-\alpha_r^2\text{tr}(\tilde{\mathbf{B}})} \left(\left(\mathbf{I} + \xi_r \tilde{\mathbf{B}} \right)^{-1} - \xi_r \left(\mathbf{I} + \xi_r \tilde{\mathbf{B}} \right)^{-1} \right. \\ & \left. \cdot \left(\mathbf{I} + \xi_r \tilde{\mathbf{B}} \right)^{-1} \cdot \tilde{\mathbf{B}} \right) + \xi_r \left(\mathbf{I} + \xi_r \tilde{\mathbf{B}} \right)^{-1} - \frac{\alpha_r^2}{1-\alpha_r^2\text{tr}(\tilde{\mathbf{B}})} \mathbf{I}. \end{aligned} \quad (7)$$

Here, \mathbf{I} is the second-order unit tensor. The parameters α_r and ξ_r represent the extensibility and mobility of the entanglement network, respectively.²¹ If these parameters are set to zero, the tensor $\mathbf{Z} = \mathbf{I}$ and Equation (6) reduces to a Neo-Hookean hardening model.

The driving stress can be decomposed into a hydrostatic σ_s^h and deviatoric part σ_s^d :

$$\sigma_s = \sigma_s^d + \sigma_s^h, \quad (8)$$

where the hydrostatic stress depends on the bulk modulus κ and the volume change ratio J as

$$\sigma_s^h = \kappa(J-1)\mathbf{I}. \quad (9)$$

For the single-mode model, the driving stress is defined by a single Maxwell mode, see Figure 1A. Hence, at small stress ($\bar{\tau} \ll \tau_0$) the relaxation time is constant, resulting in a linear elastic response up to the yield point. This means that the nonlinear preyield response is missing. To describe the complete nonlinear response, the driving stress is modeled using multiple Maxwell modes connected in parallel as shown in Figure 1B.¹⁵ Hence the name multi-mode model. Each Maxwell mode is represented by a nonlinear viscosity η_i and shear modulus G_i . Furthermore, if the deformation of the material is governed by a single molecular process, the material is called thermo-rheologically simple. Yet, for many materials this only holds in a limited range of temperatures and/or strain rates. Beyond this range of temperatures and strain rates, multiple molecular processes may contribute to the total material response, which is called a thermo-rheologically complex behavior. This can be modeled by two parallel connected sets of Maxwell elements, see Figure 1C.¹² This configuration is known as a multi-process model.

Semicrystalline polymers often reveal a thermo-rheologically complex behavior as is the case for PVDF.¹³

Therefore, the remaining equations are given for the multi-process model. Yet, in general they can be applied to all three models in Figure 1. In the multi-process model, the total deviatoric driving stress is additively decomposed into contributions of two molecular processes, whereby each process is described by a set of parallel connected nonlinear Maxwell elements. This results in the following expression of the deviatoric driving stress

$$\sigma_s^d = \sum_{i=1}^n \sigma_{s,I_i}^d + \sum_{j=1}^m \sigma_{s,II_j}^d, \quad (10)$$

where the driving stress of mode k corresponding to process π is written as

$$\sigma_{s,\pi_k}^d = G_{\pi_k} \tilde{\mathbf{B}}_{e,\pi_k}^d. \quad (11)$$

Here, G_{π_k} is the shear modulus and $\tilde{\mathbf{B}}_{e,\pi_k}^d$ the deviatoric part of the isochoric elastic left Cauchy–Green strain tensor of mode k corresponding to process π . Here, π may have the value I or II, denoting the two molecular processes that are taken into account. The subscripts $(\cdot)_n$ and $(\cdot)_m$ are the total number of modes corresponding to process I and II, respectively. Note that for a thermo-rheologically simple material corresponding to Figure 1A,B, the stress $\sigma_{s,II}^d$ vanishes.

To account for the history- and time-dependence of the material, the evolution of $\tilde{\mathbf{B}}_{e,\pi_k}$ and J are integrated over time. The corresponding kinematical evolution equations are given by

$$\dot{\tilde{\mathbf{B}}}_{e,\pi_k} = \left(\tilde{\mathbf{L}} - \mathbf{D}_{p,\pi_k} \right) \cdot \tilde{\mathbf{B}}_{e,\pi_k} + \tilde{\mathbf{B}}_{e,\pi_k} \cdot \left(\tilde{\mathbf{L}}^T - \mathbf{D}_{p,\pi_k} \right) \quad (12)$$

and

$$\dot{J} = J \text{tr}(\mathbf{D}), \quad (13)$$

where $\tilde{\mathbf{L}}$ is the isochoric velocity gradient tensor and \mathbf{D} the rate of deformation tensor. The subscript $(\cdot)^T$ denotes the transpose of a tensor. The plastic rate of deformation \mathbf{D}_{p,π_k} in mode k is related to the deviatoric driving stress through the Eyring flow viscosity η_{π_k} as

$$\mathbf{D}_{p,\pi_k} = \frac{\sigma_{s,\pi_k}^d}{2\eta_{\pi_k} \left(\bar{\tau}_{\pi_k}, p, \bar{\gamma}_{p,\pi} \right)}. \quad (14)$$

The Eyring viscosity as described in Reference 15 is used here:

$$\eta_{\pi_k} = \eta_{0,\pi_k,\text{ref}} \frac{\bar{\tau}_{\pi_k}/\tau_{0,\pi}}{\sinh(\bar{\tau}_{\pi_k}/\tau_{0,\pi})} \exp \left(\frac{\mu_{\pi_k} p}{\tau_{0,\pi}} + S_{\pi} \left(\bar{\gamma}_{p,\pi} \right) \right). \quad (15)$$

The reference viscosity of mode k is defined by $\eta_{0,\pi k,\text{ref}}$ and $\tau_{0,\pi}$ is a characteristic stress defined by the activation volume V_π^* according to Equation (16). Here, k_B is the Boltzmann constant and T the absolute temperature. The equivalent shear stress $\bar{\tau}_\pi$ is defined in Equation (17). The pressure dependence is taken into account through the parameter μ_π in combination with the hydrostatic pressure p defined in Equation (18).

$$\tau_{0,\pi} = \frac{k_B T}{V_\pi^*}, \quad (16)$$

$$\bar{\tau}_\pi = \sqrt{\frac{1}{2} \boldsymbol{\sigma}_{s,\pi}^d : \boldsymbol{\sigma}_{s,\pi}^d}, \quad (17)$$

$$p = -\frac{1}{3} \text{tr}(\boldsymbol{\sigma}). \quad (18)$$

The influence of the thermal history of the material is expressed by the parameter S_π according to Equation (19). The increase of the yield stress due to aging of the material is determined by the state parameter $S_{a,\pi}$. The softening function $R_{\gamma,\pi}$, which is a function of the equivalent plastic shear strain $\bar{\gamma}_{p,\pi}$, describes the reduction of the aged material to its rejuvenated state according to Equation (20).²⁰

$$S_\pi = S_{a,\pi} R_{\gamma,\pi}(\bar{\gamma}_{p,\pi}), \quad (19)$$

$$R_{\gamma,\pi}(\bar{\gamma}_{p,\pi}) = \left[\frac{1 + \left(r_{0,\pi} \exp(\bar{\gamma}_{p,\pi}) \right)^{r_{1,\pi}}}{1 + r_{0,\pi}^{r_{1,\pi}}} \right]^{\frac{r_{2,\pi}-1}{r_{1,\pi}}}. \quad (20)$$

The parameters $r_{0,\pi}$, $r_{1,\pi}$ and $r_{2,\pi}$ are material dependent parameters to be identified. More comprehensive expressions for the viscosity that include, for example, temperature-dependence also exist but are not used here.^{12,16}

The evolution of the equivalent plastic shear strain $\bar{\gamma}_{p,\pi}$ is defined by the mode with the longest relaxation time corresponding to process π . Under the assumption that this is the first mode for each process, the evolution is defined as:

$$\dot{\bar{\gamma}}_{p,\pi} = \frac{\bar{\tau}_{\pi 1}}{\eta_{\pi 1}}, \quad (21)$$

where $\eta_{\pi 1}$ is the viscosity of the first mode of the process and $\bar{\tau}_{\pi 1}$ is the equivalent shear stress corresponding to this mode, which is calculated using Equation (17) and the corresponding deviatoric driving stress, $\boldsymbol{\sigma}_{s,\pi 1}^d$.

The constitutive model is implemented as a UMAT user subroutine in a similar fashion as described in Reference 22. The constitutive model is used in finite element simulations which are all performed in the finite element package Abaqus CAE 2019. Details on the finite element simulations are discussed in Section 4.

3 | EXPERIMENTAL METHODS AND RESULTS

To apply the constitutive model as described in Section 2 to PVDF, the required material parameters for the model must be properly identified from experimental data. The experimental methods and results required for the parameter identification are discussed here.

3.1 | Specimens and testing methods

PVDF (Solef[®]) pellets were supplied by Solvay Specialty Polymers (Bollate, Italy). The material was prepared by compression molding: the pellets were placed in a mold, heated up to 200 °C, kept at this temperature for 15 min to allow complete melting and, finally, cooled down at a controlled rate of 10 °C/min. Several plates with different thicknesses (0.5, 4 and 8 mm) were prepared in order to extract the required specimens.

Compression specimens of $\phi 6 \times 6$ mm were prepared from the 8 mm thick plate. First, the plate was machined down to a uniform thickness of 6 mm. Subsequently, the specimens were produced. Uniaxial compression tests were performed on a Zwick 1473 universal tester, equipped with a temperature chamber and a 100 kN load cell. Tests were carried out at constant true strain rates ranging from 10^{-4} to 10^{-1} s^{-1} . PTFE spray was used to lubricate the compression plates to avoid barreling of the specimens at large strains. Because of the homogeneous deformation during the uniaxial compression tests and under the assumption of incompressibility, the true stress and true strain are computed directly from the relative displacement between the compression plates.

Dogbone tensile specimens with a nominal cross-section of $5 \times 0.5 \text{ mm}^2$, according to ISO527-1BA, were punched from the 0.5 mm thick plates. In addition, tensile specimens with a nominal cross-section of $5 \times 2.6 \text{ mm}^2$ were milled from the 4 mm thick plates that were previously machined down to a constant thickness of 2.6 mm. The geometry with corresponding dimensions is shown in Figure 2, where t indicates the thickness of the specimens. The 2.6 mm thick specimens were used for uniaxial tensile tests, whereas the 0.5 mm thick specimens were adopted for creep tests.

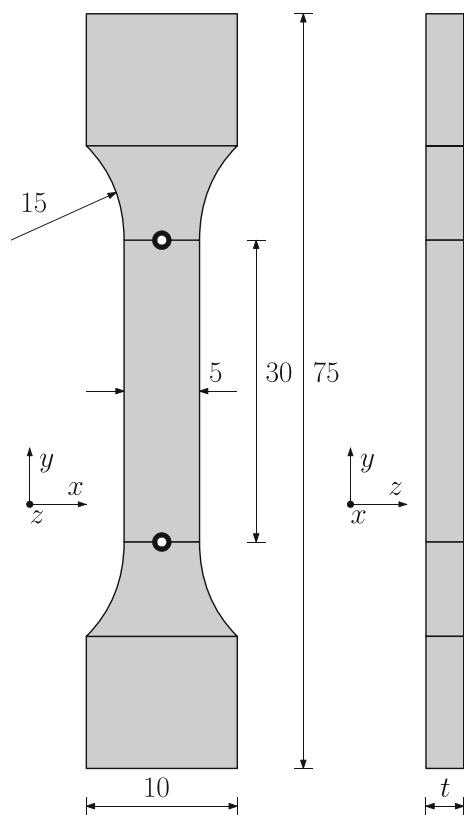


FIGURE 2 Dogbone geometry used for uniaxial tensile simulations and tensile creep simulations according to ISO527-1BA (dimensions are in millimeters).

Uniaxial tensile tests were carried out on a Zwick Z010 universal tester, equipped with a 1 kN load cell, in a temperature chamber. Deformations were measured using a non-contact extensometer (Zwick videoXtens). Tests were performed at video-controlled constant engineering strain rates between 10^{-5} and 10^{-1} s^{-1} . Adhesive markers were carefully placed along the center line of the specimens at a separating distance of approximately 30 mm. The markers are indicated by the black/white circles in Figure 2. The displacement was measured as the relative distance variation between these two gauge points. In contrast to the compression tests, the deformation during the tensile test is no longer homogeneous upon localization in the gauge section. Therefore, the engineering stress is calculated using the undeformed cross-sectional area of the tensile specimen. The engineering strain is computed from the displacement between the gauge points.

Additional creep tests were performed at different constant applied stress levels on Zwick Z010 universal testers, equipped with 1 and 10 kN load cells and in temperature chambers. In all tests the intended creep was applied within 10 s and then kept constant until failure of the specimen occurred. In this case, the strains were

simply determined from the crosshead displacement and the initial distance between the grips.

For all tests considered (compression, tensile and creep tests), three testing temperatures were used, that is 23°C (room temperature), 55 and 75°C . When the test temperature was different from room temperature, the specimens were left in the temperature chamber for 5–15 min, depending on specimen size, before starting the test in order to reach thermal equilibrium.

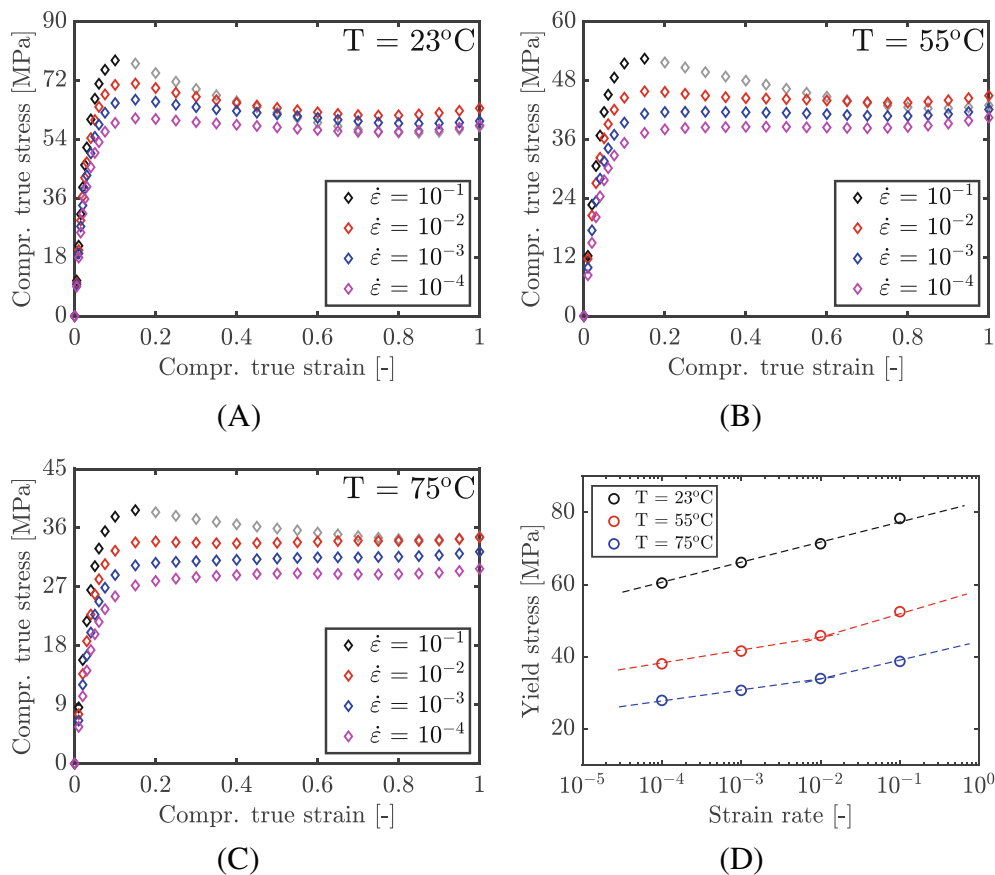
3.2 | Intrinsic stress–strain response of PVDF

For the characterization of the material parameters of the EGP-model, the intrinsic stress–strain response of the material is analyzed first. The intrinsic behavior is obtained from uniaxial compression experiments performed at different constant true strain rates and temperatures.

The true stress strain curves obtained from the experiments at three different temperatures (23 , 55 and 75°C) are shown in Figure 3A–C. At room temperature, strain softening is observed followed by moderate strain hardening for all tested strain rates. An exception is the test at strain rate $\dot{\epsilon} = 10^{-1} \text{ s}^{-1}$ where strain hardening is not noticeable. The same observation is made for the highest applied strain rate at the two other temperatures. This phenomenon is likely caused by adiabatic heating during the test, as reported by Walley et al.²³ For the lowest strain rates at 55 and 75°C , strain softening is only moderately present or not at all. The compressive yield kinetics are shown in Figure 3D where the markers are extracted from the experimental stress–strain curves. The dashed lines are interpolated to reveal the trends. The change in slope with increasing strain rate of these lines at 55 and 75°C indicate that two processes are required to describe the response over the range of applied strain rates. The strain rate at which this change in slope initiates is approximately $\dot{\epsilon} = 10^{-2} \text{ s}^{-1}$ for both temperatures. Due to the limitation of the crosshead speed of the testing equipment, higher strain rates could not be applied. Therefore, only one point could be used to indicate the change in slope. At 23°C the change in slope is not evident. However, the fact that the slope of the dashed line at 23°C is higher than the slope at 55 and 75°C , is an indication that both processes contribute to the total response over the entire range of applied strain rates at 23°C .

The wide variety in response, both for the yield kinetics and stress–strain behavior, makes it difficult to identify a unique set of parameters describing the behavior over the considered range of temperatures and strain

FIGURE 3 True stress versus true strain for uniaxial compression experiments at (A) 23 °C, (B) 55 °C and (C) 75 °C. (D) The compressive yield stress as a function of the applied true strain rate with interpolated lines to reveal the trends.



rates. This variety in response might be related to structural evolution of the material in the timespan of the experiments. Recent experimental studies into the microstructure of PVDF reported on the influence of temperature and stress on the evolution of the microscopic structure of semicrystalline PVDF. Contreras et al.²⁴ reported a decrease in crystallinity entailing a decrease in elastic modulus after stress relaxation. Zhu et al.²⁵ demonstrated that the crystallinity increases over time during annealing at elevated temperatures. Both studies show that thermomechanical loading has a significant influence on the microstructure of PVDF. To investigate the influence on the microstructure, experiments over a wide range of temperatures must be performed, and a description must be found for how the material response evolves under the influence of variable thermomechanical loading. However, for the present study and application perspective, the material behavior at the three distinct temperatures is of special interest.

Accordingly, it is not possible to identify a single set of parameters capturing the behavior of PVDF over the entire range of temperatures and strain rates using the constitutive model described in Section 2. Based on the significant difference in intrinsic response at the three temperatures in combination with the fact that the microstructure of the material changes under the

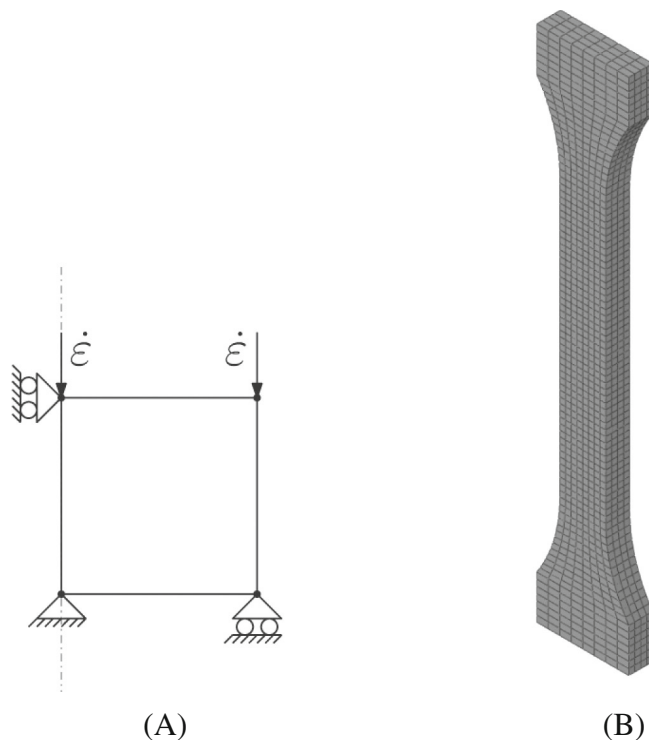


FIGURE 4 (A) Schematic representation of uniaxial compression test with boundary conditions. (B) The dogbone specimen used for the uniaxial tensile simulations discretized by 3D 8-node linear hexahedral elements.

influence of temperature, it was decided to define a distinct set of material parameters at each temperature to describe the behavior of PVDF.

4 | NUMERICAL SIMULATIONS

The details of the finite element simulations that are used in this study are discussed next.

The FE simulations of the uniaxial compression tests are performed using a single 4-node linear axisymmetric element. Uniaxial loading conditions are applied to the element following a prescribed true strain rate, taken from the experiments. A schematic representation is shown in Figure 4A, where the dashed line represents the axis of symmetry. The output parameters from the FE simulations are true stress and true strain, which can be directly compared with the experiments.

For the uniaxial tensile simulations, the geometry of the specimens that are used in the experiments is exactly reproduced, as shown in Figure 2 where the thickness t is equal to 2.6 mm. The specimen is discretized using 3D 8-node linear hexahedral elements. The corresponding mesh is shown in Figure 4B. Note that the part of the specimen that is clamped between the grips during the experiments is cut off from the geometry of the simulations. Hence, the total length of the specimen is equal to 56 mm. During the experiments, the applied strain rate is controlled using a video-extensometer which records the displacement of two gauge points located at the gauge section of the specimen. In the simulations, the displacement is prescribed at the ends of the dogbone, assuming zero slip in the grips during the experiment. However, the displacement between the gauge points should be controlled to match the applied strain rate in the experiments. Therefore, the separation between the two grips is measured during the experiments and directly applied to the ends of the specimen in the simulation. During the simulation, the displacements at the two gauge points, that are located at the same positions as those in the experiments and denoted by the two black circles in Figure 2, are monitored. These displacements are used to calculate the strain rate between the gauge points. It is verified that the applied displacement at the ends of the specimen results in a strain rate between the gauge points that is approximately equal to the strain rate applied in the experiments.

Finally, the engineering strain calculated from the FE simulations is determined from the displacements between the two gauge points. The engineering stress is determined by dividing the total reaction force at the ends of the specimen by the undeformed cross-sectional area of the gauge section.

For the tensile creep simulations, the geometry is the same as for the uniaxial tensile tests, although the specimen has a smaller thickness t , equal to 0.5 mm. The load-case in the simulations follows the same procedure as in the experiments, that is apply the load in 10 s and keep it constant afterwards. As no damage is included in the constitutive model, the specimen will not break and therefore the simulation is stopped if the engineering strain in the specimen surpasses 50%.

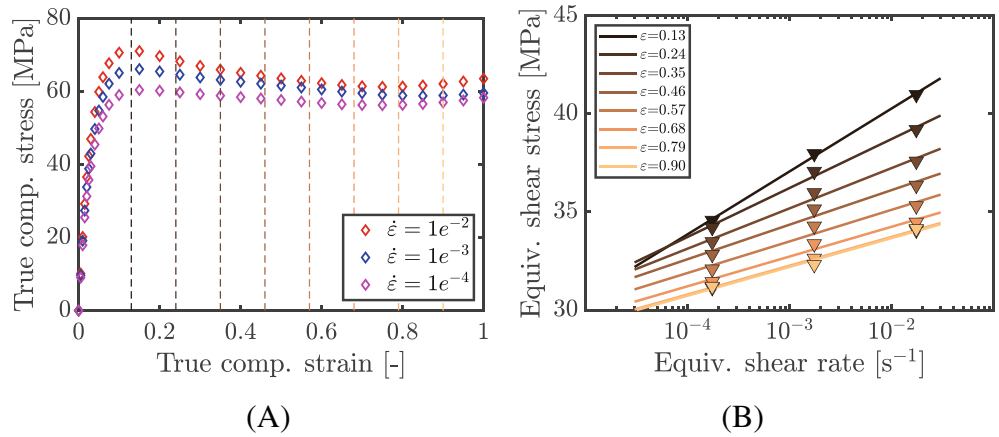
5 | CHARACTERIZATION

Three distinct sets of material parameters are identified to describe the behavior of PVDF with the EGP constitutive model, one for each temperature shown in Figure 3A–C. First, the parameters for the EGP-model as described in Section 2 are identified. Next, the proposed extension of the model is introduced to obtain a better coverage of the large strain response. The procedure for obtaining the material parameters is described in detail for the behavior at 23 °C. A similar procedure is applied to obtain the material parameters for 55 and 75 °C, which is therefore discussed briefly only.

5.1 | Intrinsic behavior at room temperature

Focusing on the experimental data for the uniaxial compression tests in Figure 3A it is clear that the rate-dependence, that is the vertical spacing between the curves, decreases with increasing strain. There are several options to describe this. Van Breemen et al.¹² demonstrated that rate-dependent strain softening in combination with two relaxation processes can be used to describe the change in rate- and temperature-dependence beyond the yield point. Applying the same procedure to PVDF does not result in a satisfactory description as it requires the presence of two molecular processes including strain softening of the secondary process. Although multiple relaxation processes occur in PVDF,^{1,26} Pini et al.¹³ showed that there is no support for the coexistence of two processes over the entire range of tested temperatures and strain rates. Also Figure 3D does not provide evidence for a change in yield kinetics at 23 °C. Therefore, a different approach is followed based on Wendlandt et al.¹⁸ and Senden et al.¹⁹ Wendlandt et al. proposed a deformation-dependent activation volume to model the large strain response of five different polymers while Senden et al. proposed the deformation-dependence of either a rate-factor or the activation volume, depending on the material of interest. To describe

FIGURE 5 (A) Compressive true stress-true strain at 23 °C. (B) Strain-rate dependence of the equivalent shear stress. Markers represent experimental data and solid lines are approximations using Equation (23).



the response of PVDF, we propose to simultaneously take into account the deformation-dependence of the rate-factor and the activation volume.

The plastic deformation rate of a thermo-rheologically simple polymer can be described by the Eyring flow rule¹⁴ as

$$\dot{\bar{\gamma}}_p = \dot{\gamma}_0 \sinh\left(\frac{\bar{\tau}V^*}{k_B T}\right), \quad (22)$$

where $\dot{\gamma}_0$ is a rate-factor denoting the thermodynamic state of the material. The remaining parameters are already defined in Section 2. The expression can be rewritten in terms of the equivalent shear stress (Equation (17)) as

$$\bar{\tau} = \frac{k_B T}{V^*} \sinh^{-1}\left(\frac{\dot{\bar{\gamma}}_p}{\dot{\gamma}_0}\right). \quad (23)$$

The equivalent shear stress at yield can approximately be described as a function of the applied strain rate using Equation (23). The parameters V^* and $\dot{\gamma}_0$, which are referred to as Eyring parameters, are determined by fitting Equation (23) to the yield stresses obtained from experiments. In the case of uniaxial compression tests performed at different applied strain rates, the stress σ and strain rate $\dot{\epsilon}$ should be converted to their shear equivalent form. This is done according to the relations $\bar{\tau} = \sigma/\sqrt{3}$ and $\bar{\gamma}_p = \sqrt{3}\dot{\epsilon}$, respectively. Considering the experimental stress-strain curves in Figure 5A, the strain at the yield point is approximately 0.13, denoted by the leftmost dashed line, where the yield point is defined as the point of maximum stress in the experiments. Applying Equation (23) to the corresponding yield stresses, results in the uppermost linear fit in Figure 5B. Beyond the yield point, it is assumed that the material behaves as a viscous fluid where the plastic strain rate is equal to the

applied strain rate. Then, Equation (23) may be applied at strains beyond the yield point, for example, the remaining vertical dashed lines in Figure 5A. This results in the corresponding linear lines in Figure 5B where the slope decreases with increasing strain. Each line represents the equivalent shear stress as a function of the equivalent shear strain rate using Equation (23), at a different strain. Accordingly, the Eyring parameters V^* and $\dot{\gamma}_0$ are now also a function of the deformation.

5.1.1 | Constant model-parameters

Although the need for deformation-dependent Eyring parameters might be necessary, the characterization procedure is initiated by assuming these parameters to be constant up to the yield point. In spite of the observation that two processes contribute to the response at 23 °C, the material is modeled as a thermo-rheologically simple material considering the linear trend of the yield kinetics at 23 °C in Figure 3D. Hence, the contribution of both processes is described by one process only using the single-process multi-mode model, according to Figure 1B. The detailed characterization is explained in multiple studies^{12,15,16,20,27} and therefore the identification of most parameters is only briefly discussed here.

The pressure dependence parameter μ_1 is determined from the difference in yield stress between compression and tensile tests at $\dot{\epsilon} = 10^{-3} \text{ s}^{-1}$.¹⁷ To this extent, the engineering yield stress obtained from the tensile test is converted to true yield stress, using $\sigma_{y,t} = \sigma_{y,e}(1 + \epsilon_e)$. Here the subscripts $(\cdot)_t$ and $(\cdot)_e$ denote the true and engineering quantities, respectively. The activation volume V_1^* , initially considered constant, is defined from the strain-rate dependence of the yield stress using the yield kinetics in Figure 3D. The parameters for modeling the Edward-Vilgis hardening stress G_T and α_T are determined by fitting Equation (6) to the large strain response of the

uniaxial compression stress as function of $|\lambda^2 - 1/\lambda|$ at $\dot{\epsilon} = 10^{-3} \text{ s}^{-1}$, where λ is the stretch ratio. The parameter ξ_r is set to zero.¹⁶ The bulk modulus κ is defined using the Young's modulus and the Poisson's ratio ν , where the latter is obtained from the data-sheet supplied by the manufacturer.

The nonlinear visco-elastic response up to the yield point is modeled by a discrete number of parallel connected Maxwell modes. The exact number of Maxwell modes that is required for an accurate description of the preyield response is unknown a priori. Van Breemen et al. introduced a procedure, to find the spectrum of relaxation times in Reference 15, using only a set of uniaxial compression or tension experiments performed at varying constant strain rates. This procedure is based on the principle of time-stress superposition, and for a detailed description, the reader is referred to Reference 15. It is assumed that all modes in the spectrum are related to process I. However, the procedure can also be applied to process II, as long as the stress of process II is isolated from the total stress. The total relaxation modulus E as function of time t for n parallel connected Maxwell elements is defined as

$$E_1(t) = \sum_{i=1}^n E_{i1} \exp\left(-\frac{t}{\lambda_{i1}}\right), \quad (24)$$

where E_{i1} and λ_{i1} are the relaxation modulus and relaxation time of Maxwell mode i , respectively, and n is an arbitrary number representing the total number of modes. The stress response of multiple Maxwell elements in parallel can be expressed in its 1D form by a Boltzmann integral. Substitution of Equation (24) into the Boltzmann integral results in the following expression for the driving stress:

$$\sigma_{s,I}(t) = \sum_{i=1}^n \left[E_{i1} \dot{\epsilon} \int_{-\infty}^t \exp\left(-\frac{\Psi - \Psi'}{\lambda_{i1}}\right) dt' \right]. \quad (25)$$

Here, $\sigma_{s,I}(t)$ is the driving stress as a function of time t . Further, Ψ and Ψ' are stress-reduced times that are calculated by integration of a stress-shift factor $a_\sigma(\sigma)$. The required number of modes n is still unknown, and therefore a discrete spectrum of relaxation times λ_{i1} is defined. The range of relaxation times is defined by the stress-reduced time Ψ . Subsequently, a least-squares fit of Equation (25) is performed on the preyield regime of the experimental driving stress-strain response at a single strain rate. This results in a spectrum of n relaxation moduli E_{i1} and relaxation times λ_{i1} , where the least-squares method determines the number of modes n required to adequately describe the experimental stress.

Finally, the relaxation moduli are converted to shear moduli G_{i1} and the reference viscosities are calculated according to Equation (26).

$$\eta_{0,I,ref} = \lambda_{i1} \times G_{i1} \exp(-S_{a,I}). \quad (26)$$

The factor $\exp(-S_{a,I})$ results in a shift of all viscosities along the time-axis to the reference state, since the spectrum that is determined from the experimental driving stress is related to an aged material. The result is the spectrum of relaxation moduli G_{i1} and reference viscosities $\eta_{0,I,ref}$.

Applying this procedure to the compressive driving stress-strain curve obtained at a constant strain rate $\dot{\epsilon} = 10^{-3} \text{ s}^{-1}$ results in a good description of the preyield regime, see Figure 6A. The discrete spectrum consists of $n = 21$ modes of which the shear moduli and reference viscosities are shown in Table A1. The individual relaxation modes and the total relaxation modulus are shown in Figure 6B.

The state parameter $S_{a,I}$ is used to describe the increase of the yield stress due to aging of the material. The increase of the yield stress is usually followed by softening of the material. However, hardly any strain softening is observed for the lowest applied strain rate in Figure 3A. Furthermore, the experiments were conducted right after the samples were prepared, resulting in a minimal aging time. Therefore, the state parameter $S_{a,I}$ and the softening parameters $r_{0,I}$, $r_{1,I}$ and $r_{2,I}$ are set equal to zero. The identified parameters are summarized in Table 1.

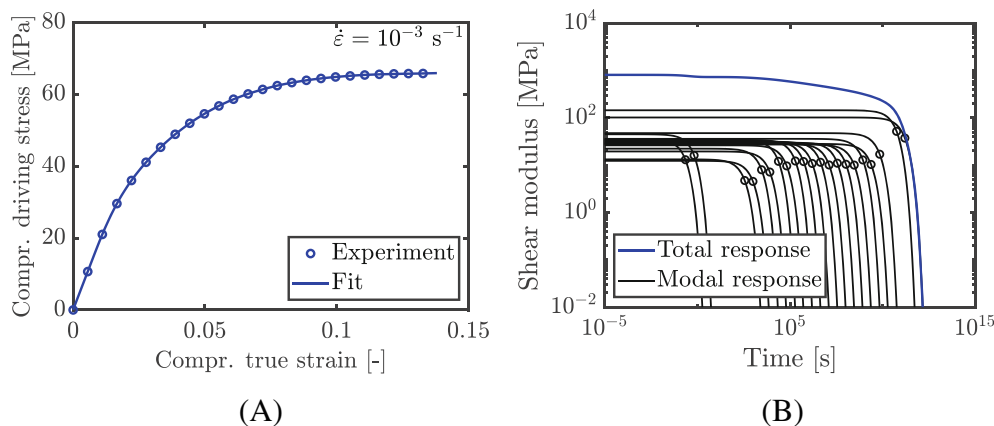
5.1.2 | Strain-dependent Eyring parameters

The next step is to define the evolution of the Eyring parameters with deformation. The strain-dependence of the Eyring parameters is of influence on the driving stress only. Therefore, Equation (23) is rewritten into the shear equivalent driving stress $\bar{\tau}_s$ as

$$\bar{\tau}_s = \frac{k_B T}{V^*} \sinh^{-1} \left(\frac{\dot{\gamma}_p}{\dot{\gamma}_0} \right). \quad (27)$$

From the experiments, the compressive driving stress is determined by subtracting the hardening stress, described by Equation (6), from the total stress. The compressive driving stress is then converted to the shear equivalent driving stress according to $\bar{\tau}_s = \sigma_s / \sqrt{3}$. The Eyring parameters $\dot{\gamma}_0$ and V^* are determined by performing a least-squares fit on the experimental shear equivalent driving stress with Equation (27) for a sequence of strains. Under the assumption that $\bar{\tau}_p = 0$ at the

FIGURE 6 (A) Compressive true driving stress described by the discrete modes displayed in Table A1 (solid line) compared with the experiment (markers). (B) The corresponding relaxation spectrum where individual modes are displayed in black and the total relaxation modulus in blue.



compressive yield point, the Eyring parameters are dependent on the equivalent plastic shear strain, where $\bar{\gamma}_p = \sqrt{3}\epsilon_p$ for uniaxial compression. Applying this procedure to the experimental driving stress, results in the deformation-dependent activation volume $V^*(\bar{\gamma}_p)$ and rate-factor $\dot{\gamma}_0(\bar{\gamma}_p)$.

To incorporate these strain-dependencies in the constitutive model described in Section 2, first the reference viscosity η_0 is determined according to Equation (28).

$$\eta_0(\bar{\gamma}_p) = \frac{k_B T}{V^*(\bar{\gamma}_p) \dot{\gamma}_0(\bar{\gamma}_p)}. \quad (28)$$

The values for the activation volume and the reference viscosity at different levels of equivalent plastic shear strain are shown by the blue markers in Figure 7.

A mathematical function is defined to approximate the strain-dependence in Equation (27). The bilinear descriptions defined in Equations (29) and (30) are proposed to capture the dependencies on the equivalent plastic shear strain. The functions are denoted by the solid lines in Figure 7.

$$V^*(\bar{\gamma}_p) = \begin{cases} V_s^* + \Phi_V \bar{\gamma}_p & 0 \leq \bar{\gamma}_p < \bar{\gamma}_{p,t}, \\ V^*(\bar{\gamma}_p = \bar{\gamma}_{p,t}) & \bar{\gamma}_p \geq \bar{\gamma}_{p,t}, \end{cases} \quad (29)$$

$$\eta_0(\bar{\gamma}_p) = \begin{cases} 10^{[\Phi_{\eta_0} \bar{\gamma}_p + \log(\eta_{0,s})]} & 0 \leq \bar{\gamma}_p < \bar{\gamma}_{p,t}, \\ \eta_0(\bar{\gamma}_p = \bar{\gamma}_{p,t}) & \bar{\gamma}_p \geq \bar{\gamma}_{p,t}. \end{cases} \quad (30)$$

Here, V_s^* and $\eta_{0,s}$ represent the corresponding values at $\bar{\gamma}_p = 0$ and $\bar{\gamma}_{p,t}$ denotes the equivalent plastic shear strain at which the parameters remain constant. Φ_V is the slope of the $(V^*, \bar{\gamma}_p)$ -curve and Φ_{η_0} the slope of the $(\log(\eta_0), \bar{\gamma}_p)$ -curve. The values of these parameters are summarized in Table 2. The value of η_0 at the yield point,

TABLE 1 Parameters of process I for PVDF at $T = 23$ °C.

Parameter	Value	Unit
V_1^*	$2.94 \cdot 10^{-27}$	(m ³)
μ_1	0.175	(-)
G_r	0.6	(MPa)
α_r	0.25	(-)
κ	$1.8 \cdot 10^3$	(MPa)
$\sum_{i=1}^n \eta_{0,i,ref}$	$2.45 \cdot 10^{13}$	(MPa·s)

that is $\bar{\gamma}_p = 0$, should equal the sum of all reference viscosities contained in the spectrum of relaxation times. Therefore, the reference viscosities in the spectrum are scaled with respect to $\eta_0(\bar{\gamma}_p = 0)$ according to Equation (31).

$$\eta_{0,i,k,ref}(\bar{\gamma}_p) = \eta_{0,i,k,ref,init} \frac{\eta_0(\bar{\gamma}_p)}{\eta_{0,s}}, \quad (31)$$

where $\eta_{0,i,k,ref,init}$ are the unscaled reference viscosities in the spectrum, defined using the procedure described in Section 5.1.1.

The original model described in Section 2 is extended with Equations (29)–(31). Consequently, the following equations from the original model are redefined as they become strain-dependent. First, the strain-dependence of the activation volume results in a strain-dependent characteristic stress $\tau_{0,\pi}$, that is, Equation (16) is now written as

$$\tau_{0,\pi}(\bar{\gamma}_p) = \frac{k_B T}{V_\pi^*(\bar{\gamma}_p)}, \quad (32)$$

where $V_\pi^*(\bar{\gamma}_p)$ is defined according to Equation (29). Second, the strain-dependence of the reference viscosity

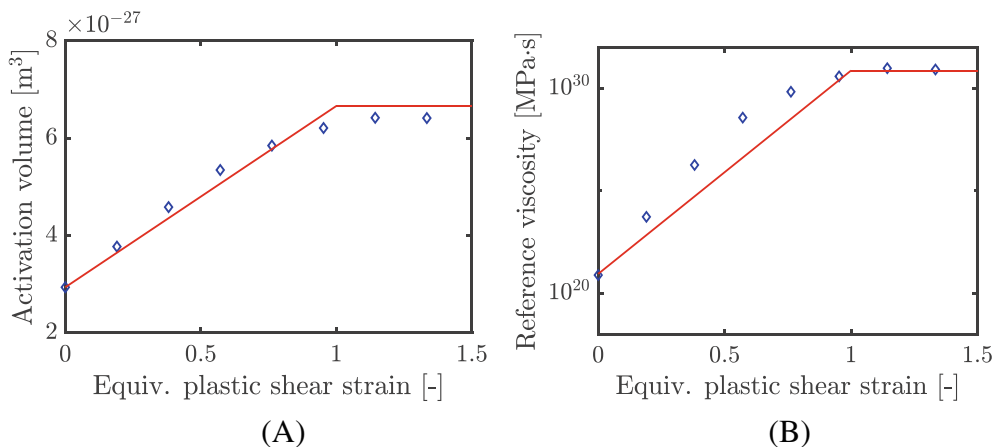


FIGURE 7 (A) Evolution of the activation volume and (B) the reference viscosity as function of the equivalent plastic shear strain, described by Equations (29) and (30), respectively. Blue markers are the corresponding values obtained using experimental data and Equation (27).

TABLE 2 Parameters to describe the strain-dependence of the Eyring parameters for PVDF at $T = 23^\circ\text{C}$.

Parameter	Value	Unit
V_s^*	$2.94 \cdot 10^{-27}$	(m^3)
Φ_V	$3.73 \cdot 10^{-27}$	(m^3)
$\eta_{0,s}$	$8.83 \cdot 10^{20}$	($\text{MPa}\cdot\text{s}$)
Φ_{η_0}	9.93	($\text{MPa}\cdot\text{s}$)
$\bar{\gamma}_{p,t}$	1.0	(-)

results in the strain-dependence of the Eyring viscosity η_{π_k} , that is, Equation (15) is now written as

$$\eta_{\pi_k}(\bar{\gamma}_p) = \eta_{0,\pi_k,\text{ref}}(\bar{\gamma}_p) \frac{\bar{\tau}_\pi / \tau_{0,\pi}(\bar{\gamma}_p)}{\sinh(\bar{\tau}_\pi / \tau_{0,\pi}(\bar{\gamma}_p))} \exp\left(\frac{\mu_\pi P}{\tau_{0,\pi}(\bar{\gamma}_p)} + S_\pi(\bar{\gamma}_{p,\pi})\right), \quad (33)$$

where $\eta_{0,\pi_k,\text{ref}}(\bar{\gamma}_p)$ is defined in Equation (31). All remaining equations in Section 2 are unaffected by the strain-dependence of the activation volume and the reference viscosity.

Equations (29)–(33) are implemented in the constitutive model. Finite element simulations of uniaxial compression tests are then compared with experiments, to verify whether the intrinsic response of PVDF can be described by the proposed strain-dependence of the Eyring parameters. The comparison between the FE simulations and the experiments is shown in Figure 8A. The spectrum of relaxation times accurately describes the visco-elastic preyield response. Although the strain-dependence of the Eyring parameters according to Equations (29) and (30) is a simplified description, the strain rate-dependence of the postyield response is described very well. The preyield

response at $\dot{\epsilon} = 10^{-1} \text{ s}^{-1}$ is slightly underpredicted because the additional contribution of another process might be active here, as reported in Reference 13. Yet, the yield kinetics of the experiments as compared with the simulations in Figure 8D reveal an accurate description using only one process. Note that the deviation of the large-strain response at the highest strain rate in Figure 8A is due to adiabatic heating during the experiment which is not accounted for in the simulations. Nevertheless, the identified parameters in combination with their strain-dependence result in an adequate description of the stress–strain response at 23°C .

5.2 | Intrinsic behavior at 55 and 75 °C

The same procedure is followed to identify the material parameters for the single-process multi-mode model (Figure 1B) at 55 and 75 °C. The resulting material parameters are summarized in Table 3. The spectra of relaxation modes are characterized on the compressive driving stress–strain curve obtained at a constant strain rate $\dot{\epsilon} = 10^{-3} \text{ s}^{-1}$ for both temperatures. This results in two spectra, each containing $n = 18$ relaxation modes, which can be found in Appendix A. The state parameter $S_{a,I}$ and the softening parameters $r_{0,I}$, $r_{1,I}$ and $r_{2,I}$ are set to zero for these temperatures as well. Similarly, FE simulations at different constant true strain rates are performed to assess the predictive nature of the parameters. The results are compared with the experiments in Figure 8B,C. For both temperatures, the deformation-dependent Eyring parameters yield a good description of the intrinsic response. Although Equations (29) and (30) are defined based on experimental data obtained at 23°C , the equations can adequately describe the response at 55 and 75 °C with the correct parameters from Table 3. The predicted yield point however is lower than the experimental yield point for the highest applied strain

FIGURE 8 (A–C) Uniaxial compression simulations (solid lines) compared with experiments (markers) at 23, 55 and 75 °C, respectively, using the extended constitutive model in the single-process multi-mode form. (D) Yield kinetics for the uniaxial compression tests, where the experimental data is represented by the round markers and simulation results by triangular markers.

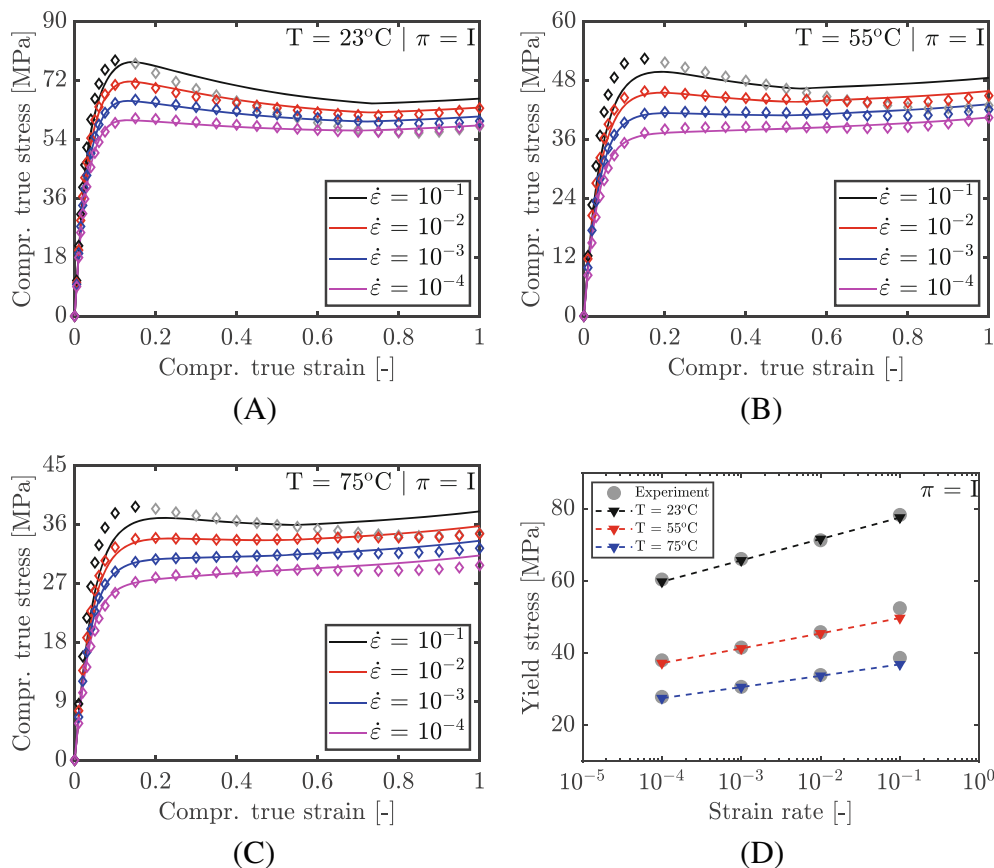


TABLE 3 Material parameters for PVDF at $T = 55$ and 75 °C.

Parameter	55 °C	75 °C	Unit
V_I^*	$4.18 \cdot 10^{-27}$	$5.95 \cdot 10^{-27}$	(m ³)
μ_I	0.1	0.1	(–)
G_r	0.6	0.6	(MPa)
α_r	0.25	0.25	(–)
κ	$1.8 \cdot 10^3$	$1.8 \cdot 10^3$	(MPa)
$\sum_{i=1}^n \eta_{0,i,ref}$	$3.29 \cdot 10^{11}$	$1.80 \cdot 10^{11}$	(MPa·s)
V_s^*	$4.18 \cdot 10^{-27}$	$5.95 \cdot 10^{-27}$	(m ³)
Φ_V	$4.55 \cdot 10^{-27}$	$4.78 \cdot 10^{-27}$	(m ³)
$\eta_{0,s}$	$2.72 \cdot 10^{18}$	$1.62 \cdot 10^{18}$	(MPa·s)
Φ_{η_0}	8.45	6.62	(MPa·s)
$\bar{\gamma}_{p,t}$	0.65	0.65	(–)
V_{II}^*	$5.8 \cdot 10^{-27}$	$5.8 \cdot 10^{-27}$	(m ³)
μ_{II}	0.02	0.02	(–)
$S_{a,II}$	4.0	4.0	(–)
$r_{0,II}$	0.97	0.97	(–)
$r_{1,II}$	50.0	50.0	(–)
$r_{2,II}$	–5.0	–5.0	(–)
G_{II}	$8.02 \cdot 10^1$	$8.02 \cdot 10^1$	(MPa)
$\eta_{0,II,ref}$	$4.76 \cdot 10^{-2}$	$4.76 \cdot 10^{-2}$	(MPa·s)

rate. In Figure 8D the yield kinetics for the simulations and the experiments are shown. The fact that for 55 and 75 °C at high strain rates, the yield stress in the simulations is lower than those in the experiments, clearly indicates that the contribution of a second process is missing in the simulations. At 23 °C this is not the case because the contribution of both processes is described by one process. Therefore, the parameters for process II are identified for these two temperatures next.

5.2.1 | Thermo-rheologically complex material

To describe the yield kinetics of PVDF at 55 and 75 °C for strain rates higher than $\dot{\epsilon} = 10^{-2} \text{ s}^{-1}$, two processes are required. The addition of an extra process means that the behavior at 55 and 75 °C is modeled using the multi-process multi-mode model as shown in Figure 1C. The parameters for process I, previously defined and shown in Table 3 remain the same, and therefore only the parameters for process II must be defined. The parameters for process II are determined from the experimental stress–strain curves at a constant strain rate $\dot{\epsilon} = 10^{-1} \text{ s}^{-1}$. The response of process II is isolated from the total response by subtracting the response of process I,

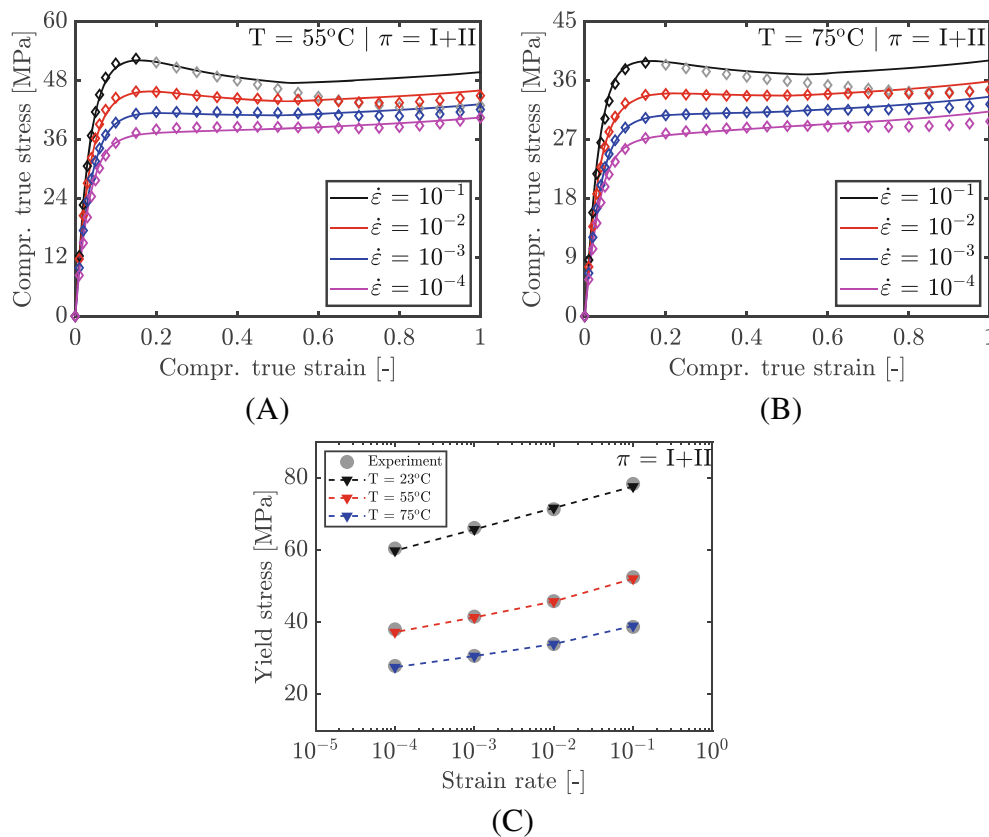


FIGURE 9 (A, B) Uniaxial compression simulations (solid lines) compared with experiments (markers) at 55 and 75 °C, respectively, using the extended constitutive model in the multi-process form. (C) Corresponding yield kinetics for the uniaxial compression tests, where the experimental data is represented by the round markers and simulation results by triangular markers.

obtained from FE simulations, from the total response. The uniaxial compression test at $\dot{\epsilon} = 10^{-1} \text{ s}^{-1}$ reveals signs of adiabatic heating. Therefore, only the data up to the yield point is used for the identification of the parameters.

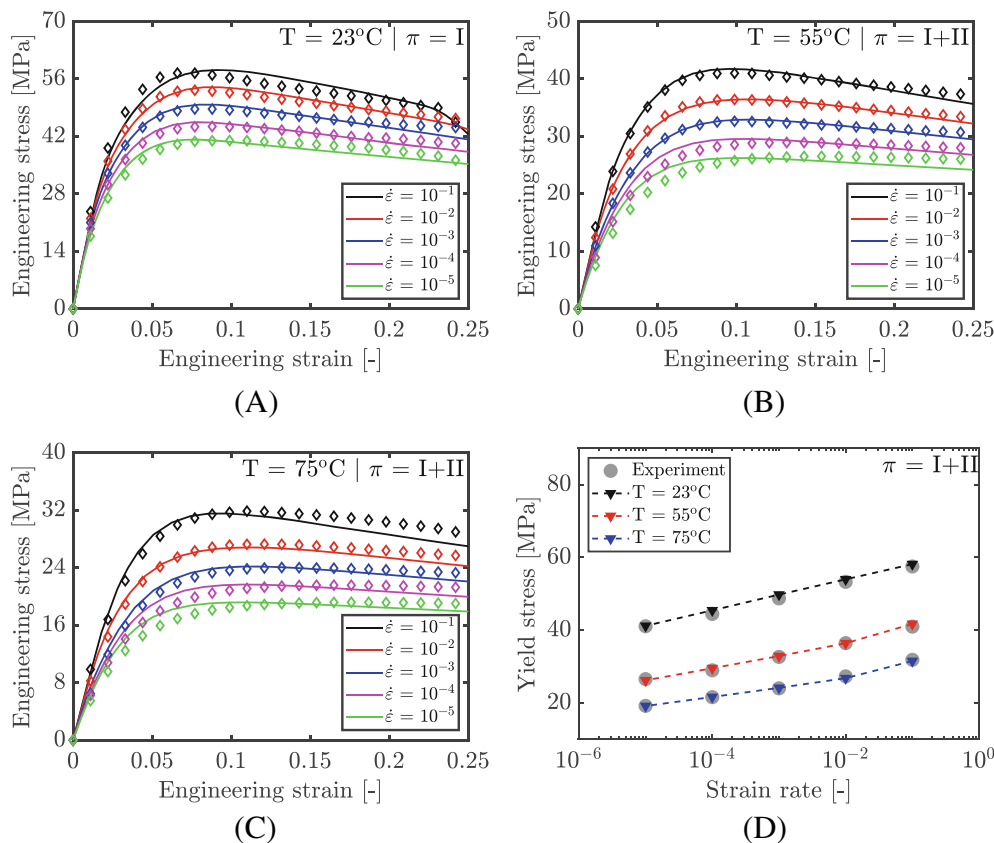
The pressure dependence of process II is determined from the difference in yield stress between uniaxial compression and tension at $\dot{\epsilon} = 10^{-1} \text{ s}^{-1}$. Only one additional Maxwell mode is required to describe the contribution of process II, that is, $m = 1$ in Equation (10). In Reference 12 the contribution of a second process in the EGP-model has been assessed. It was thereby concluded that the equivalent plastic shear strain is equal for all processes, meaning that the onset of yield is equal for all processes. The difference between experiment and simulation in Figure 8B shows that the contribution of process II should vanish right after the yield point of process I. This means that process II should start to yield at lower strains than process I. Therefore, we assume that the softening of process II depends on the viscous deformation related to process II, $\bar{\gamma}_{p,II}$, of which the evolution is described by Equation (21). In addition, the state parameter $S_{a,II}$ and the softening parameters $r_{0,II}$, $r_{1,II}$ and $r_{2,II}$ are defined such that the contribution of the second process vanishes right after the yield point of process I. All parameters related to process II are summarized in Table 3. Because process II only contributes to the total stress up to the yield point and the Eyring parameters are assumed to be

constant up to the yield point, the Eyring parameters corresponding to process II are constant with deformation. Finally, FE simulations are performed with both processes for all strain rates. The results are shown in Figure 9A,B. It is clear that the addition of process II improves the preyield description for the highest strain rates, whereas it has hardly any influence on the post-yield response. The yield kinetics extracted from the simulations are shown in Figure 9C from which it can be concluded that the addition of a second process at 55 and 75 °C results in a better description at high strain rates. Note that at 23 °C still only one process is used.

6 | VALIDATION

In the previous section it is shown that with the strain-dependence of the Eyring parameters, the intrinsic response of PVDF can be described over a wide range of strain rates. To validate whether this is also predictive in different loading geometries or loadcases, two validation studies are performed at all three temperatures. It is important to make a distinction between the experiments used for characterization and validation. For the characterization of the model parameters, the following experiments were used for all three temperatures: uniaxial compression tests at strain rates $\dot{\epsilon} = 10^{-4}$ to $\dot{\epsilon} = 10^{-1} \text{ s}^{-1}$

FIGURE 10 (A–C) Engineering stress versus strain for uniaxial tensile tests at 23, 55, and 75 °C, respectively. The results obtained from simulations are denoted by solid lines, experiments are represented by markers. (D) Yield kinetics for the uniaxial tensile tests, where the experimental data is represented by the round markers and simulation results by triangular markers.



and a uniaxial tensile test at $\dot{\epsilon} = 10^{-3}$. A uniaxial tensile test $\dot{\epsilon} = 10^{-1} \text{ s}^{-1}$ was also used to determine the properties for process II at 55 and 75 °C. All remaining tensile tests and creep tests described in Section 3.1 are only used for the validation of the model. Hence, no additional parameters have been characterized for the simulations described in this section.

6.1 | Uniaxial tensile simulations

First, FE simulations of uniaxial tensile tests at a constant prescribed engineering strain rate are performed. The results are compared with experimental data. Note that in contrast to the uniaxial compression tests where a true strain rate is used, for the tensile tests the engineering strain rates are used.

The validation simulations are performed at the three experimental temperatures. The constant applied strain rates vary from $\dot{\epsilon} = 10^{-5}$ to $\dot{\epsilon} = 10^{-1} \text{ s}^{-1}$. For the simulations at 55 and 75 °C, the parameters for processes I and II are used, listed in Table 3. For the simulation at 23 °C, the parameters listed in Tables 1 and 2 are used. The engineering stresses versus engineering strains are plotted in Figure 10A–C where the simulations are denoted by the solid lines and the experimental data is shown by the markers. The predicted response from the simulations is somewhat higher for the lowest two strain rates in the preyield range at all temperatures. At 75 °C the

predicted response at large strains is slightly lower than the experiments, especially at the highest applied strain rate. Looking at the tensile yield kinetics in Figure 10D it can be concluded that for all temperatures the yield stress is predicted very well. In conclusion, the simulations are in adequate agreement with the experimental results over a wide range of applied strain rates.

During some of the uniaxial tensile experiments, total failure of the specimen was preceded by the formation of a stable neck. Due to imperfections in the specimen, strain localization can occur which results in the concentration of large plastic deformations at the imperfection. If this localization stabilizes due to strain hardening, stable neck growth along the specimen takes place up to the point that the specimen fractures. This phenomenon is also observed in the simulations. For example at the two highest strain rates at 23 °C, note the sharp decrease in stress in Figure 10A. However, the number of specimens that showed neck formation during the experiments is too low in order to give a reliable comparison with simulations.

6.2 | Tensile creep simulations

Part of the uniaxial tensile tests were used for the characterization of the parameters. For this reason, an extra validation case is performed in the form of tensile creep simulations.

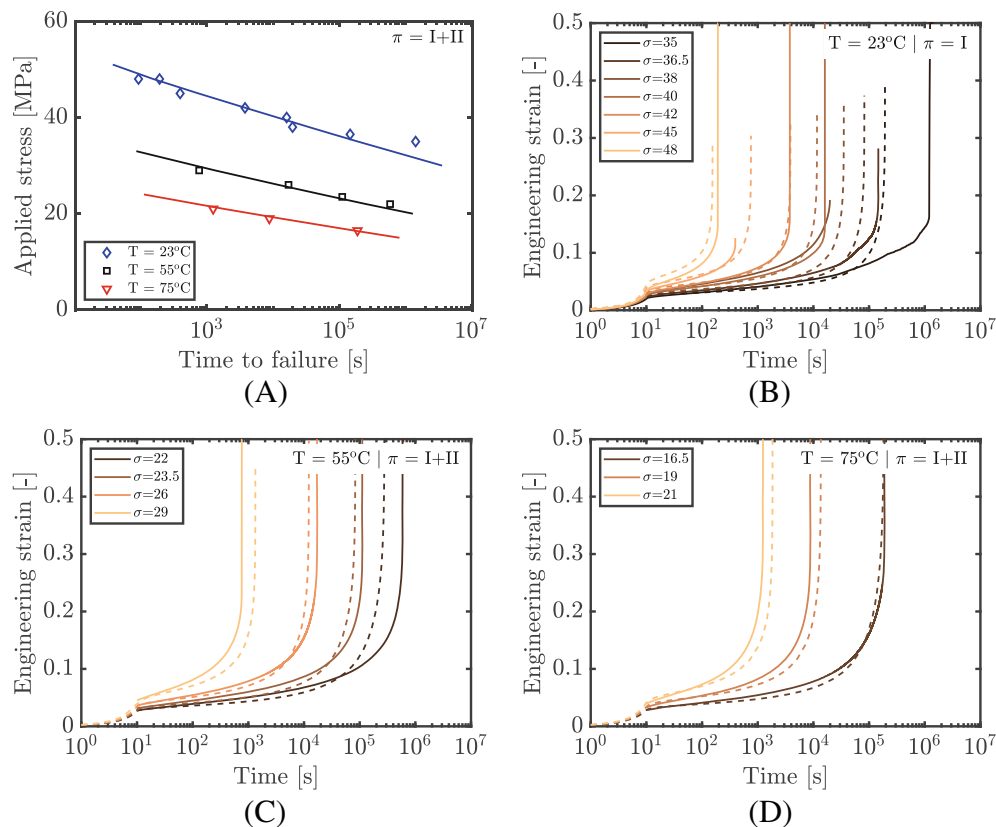


FIGURE 11 (A) Time-to-failure as function of the applied stress for tensile creep simulations at three different temperatures where markers indicate experimental results. (B–D) Time-strain plots of tensile creep simulations (dashed lines) compared with experiments (solid lines) at a temperature of 23, 55 and 75 °C, respectively.

For each experiment, the applied stress is plotted as function of the time-to-failure, represented by the markers in Figure 11A. The solid lines are the predictions by the FE simulations. The time-to-failure for both experiments and simulations are taken at the time instance at which the engineering strain equals 20%. Clearly, the constitutive model well predicts the time-to-failure over a wide range of applied stresses for all three temperatures.

The engineering strains versus time at different temperatures are shown in Figure 11B–D where the experiments are shown by the solid lines and the simulations are given by the dashed lines. The decrease of the slope of the curve after 10 s is a result of the load being kept constant from that point in time. The region of constant plastic flow, marked by the more or less constant shallow slope of the curve, is called the secondary creep region. The slope in this region is equal to the plastic flow rate. Comparing the simulations to the experiments, the lines in this region result in an adequate match. Secondary creep is followed by a region of increasing plastic strain rate up to the point that strain localization occurs and the specimen fails. The onset of failure is apparent from the nearly vertical increase of strain. Comparing the vertical increase of simulations to experiments, a good match is again observed. At 23 °C the deviation from the experimental results seems to be slightly increasing with decreasing applied stress. However, note that especially for an applied stress of 35 MPa there is some experimental uncertainty as visible through

the nonsmooth increase of the experimental engineering strain (rightmost solid line).

6.3 | Discussion

As it was necessary to identify different sets of parameters at distinct temperatures, the set representing one temperature is not applicable to other temperatures. Nevertheless, the strategy described in Section 5 can also be applied to model the material behavior at different temperatures. This requires an additional identification of the dependence of the parameters on the temperature. It is then dependent on the desired temperature, how many processes must be incorporated in the model. It is expected that for higher temperatures, only one relaxation process is required.¹³ Nevertheless, the established extension of the constitutive model enables the user to apply a similar procedure at different temperatures.

The original model as described in Section 2 is able to describe the temperature-dependent intrinsic behavior of polymers using only one set of parameters. In this study it is shown that different sets of parameters are needed to describe the intrinsic behavior of PVDF at different temperatures. However, as explained in Section 3.2, this is due to the complex behavior of PVDF. In case of a different material, it is possible that the extended model can describe the temperature-dependent intrinsic behavior

using a single set of parameters. In that case, the temperature-dependence of the Eyring viscosity in Equation (33) must be taken into account. Hence, the fact that in this study different sets of material parameters are used is only related to the material that is described, PVDF, and is not a limitation of the extended model.

7 | CONCLUSIONS

In this article, the elasto-viscoplastic constitutive model presented by van Breemen et al.¹² is extended to describe the temperature-, time- and rate-dependent behavior of PVDF. The proposed extension incorporates the deformation-dependent evolution of the Eyring parameters which is required to capture the intrinsic response of PVDF. The required material parameters for the extended model are identified at three temperatures (23, 55 and 75 °C) using uniaxial compression and tensile tests at different strain rates. After identifying different sets of material parameters at three different temperatures, the model is used in FE simulations to predict the intrinsic response of PVDF, which reveals a remarkably good agreement between experiments and simulations. The model and parameter sets are validated by assessing the response of uniaxial tensile tests and tensile creep tests which were not used for the parameter identification. Comparison of the FE simulations with the experimental results reveals a convincing predictive capacity of the extended model. In conclusion, the extended model is able to predict the short- and long-term rate-dependent material behavior of PVDF at different temperatures for different loading conditions.

ACKNOWLEDGMENTS

The authors thank Shell Global Solutions International B.V. for their support, Solvay for their kind assistance in supplying the materials and J. van Hout, MSc for help in the experimental part of this work.


ORCID

Tom Lenders  <https://orcid.org/0000-0002-9763-5648>

Joris J. C. Remmers  <https://orcid.org/0000-0001-5823-2558>

Tommaso Pini  <https://orcid.org/0000-0002-0615-9384>

Leon E. Govaert  <https://orcid.org/0000-0002-7557-8443>

Marc G. D. Geers  <https://orcid.org/0000-0002-0009-6351>

REFERENCES

- [1] V. Sencadas, R. Gregorio Jr., S. Lanceros-Méndez, *J. Macromol. Sci., Part B: Phys.* **2009**, *48*, 514.
- [2] S. Castagnet, J.-L. Gacougnolle, P. Dang, *Mater. Sci. Eng., A* **2000**, *276*, 152.
- [3] N. von Solms, N. Zecchin, A. Rubin, S. I. Andersen, E. H. Stenby, *Eur. Polym. J.* **2005**, *41*, 341.
- [4] M. Tamura, K. Ogasawara, N. Ono, S. Hagiwara, *J. Appl. Phys.* **1974**, *45*, 3768.
- [5] M. G. Broadhurst, G. T. Davis, J. E. McKinney, *J. Appl. Phys.* **1978**, *49*, 4992.
- [6] G. M. Sessler, *J. Acoust. Soc. Am.* **1981**, *70*, 1596.
- [7] J. M. L. Reis, E. P. Motta, H. S. da Costa Mattos, *Polym. Test.* **2015**, *46*, 9.
- [8] E. P. Motta, J. M. L. Reis, H. S. da Costa Mattos, *Polym. Test.* **2018**, *67*, 503.
- [9] M. Challier, J. Besson, L. Laiarinandrasana, R. Piques, *Eng. Fract. Mech.* **2006**, *73*, 79.
- [10] L. Laiarinandrasana, J. Besson, M. Lafarge, G. Hochstetter, *Int. J. Plast.* **2009**, *25*, 1301.
- [11] J. O'Connor, B. Bastos dos Santos, L. Borges, M. Ferreira da Costa, D. Alves Castello, *J. Braz. Soc. Mech. Sci. Eng.* **2020**, *42*, 438.
- [12] L. C. A. van Breemen, T. A. P. Engels, E. T. J. Klompen, D. J. A. Senden, L. E. Govaert, *J. Polym. Sci., Part B: Polym. Phys.* **2012**, *50*, 1757.
- [13] T. Pini, M. van Drongelen, J. J. C. Remmers, M. G. D. Geers, L. E. Govaert, *J. Polym. Sci.* **2021**, *59*, 1209.
- [14] H. Eyring, *J. Chem. Phys.* **1936**, *4*, 283.
- [15] L. C. A. van Breemen, E. T. J. Klompen, L. E. Govaert, H. E. H. Meijer, *J. Mech. Phys. Solids* **2011**, *59*, 2191.
- [16] D. J. A. Senden, S. Krop, J. A. W. van Dommelen, L. E. Govaert, *J. Polym. Sci., Part B: Polym. Phys.* **2012**, *50*, 1680.
- [17] C. C. W. J. Clarijs, L. E. Govaert, *J. Polym. Sci., Part B: Polym. Phys.* **2019**, *57*, 1001.
- [18] M. Wendlandt, T. A. Tervoort, U. W. Suter, *Polymer* **2005**, *46*, 11786.
- [19] D. J. A. Senden, J. A. W. van Dommelen, L. E. Govaert, *J. Polym. Sci., Part B: Polym. Phys.* **2010**, *48*, 1483.
- [20] E. T. J. Klompen, T. A. P. Engels, L. E. Govaert, H. E. H. Meijer, *Macromolecules* **2005**, *38*, 6997.
- [21] S. F. Edwards, T. Vilgis, *Polymer* **1986**, *27*, 483.
- [22] UMAT, *Abaqus User Subroutines Reference Manual. Version 6.12*, Dassault Systemes Simulia Inc., **2012**.
- [23] S. M. Walley, J. E. Field, P. H. Pope, N. A. Safford, *Philos. Trans. Royal Soc. London Ser. A, Math. Phys. Sci.* **1989**, *328*, 1.
- [24] M. M. Contreras, C. R. Nascimento, R. P. Cucinelli Neto, S. Teixeira, N. Berry, M. F. Costa, C. A. Costa, *Polym. Test.* **2018**, *68*, 153.
- [25] Y. Zhu, H. Ye, L. Yang, L. Jiang, L. Zhen, J. Huang, Z. Jiao, J. Sun, *Polym. Polym. Compos.* **2016**, *24*, 167.
- [26] J. S. Harrison, Z. Ounaies, Piezoelectric polymers. *NTRS-NASA Technical Reports Server*. Report No. 2001-43.
- [27] T. A. P. Engels, L. E. Govaert, H. E. H. Meijer, Mechanical characterization of glassy polymers: quantitative prediction of their short- and long-term responses. *Polymer Science: A Comprehensive Reference*, **2012**, *2*, 723.

How to cite this article: T. Lenders, J. J. C. Remmers, T. Pini, P. Veenstra, L. E. Govaert, M. G. D. Geers, *J. Polym. Sci.* **2023**, *61*(14), 1439. <https://doi.org/10.1002/pol.20220729>

APPENDIX A: SPECTRA OF RELAXATION MODES

The spectra of relaxation modes, consisting of the shear moduli and reference viscosities for the three different temperatures are shown here (Tables A1, A2 and A3).

TABLE A1 Spectrum of relaxation moduli and reference viscosities of process I for PVDF at $T = 23\text{ }^{\circ}\text{C}$.

Mode nr. (-)	Shear modulus G_i (MPa)	Viscosity $\eta_{0,i,\text{ref}}$ (MPa·s)
1	$1.02 \cdot 10^2$	$1.61 \cdot 10^{13}$
2	$1.45 \cdot 10^2$	$8.01 \cdot 10^{12}$
3	$4.75 \cdot 10^1$	$3.23 \cdot 10^{11}$
4	$2.81 \cdot 10^1$	$6.70 \cdot 10^{10}$
5	$3.60 \cdot 10^1$	$3.00 \cdot 10^{10}$
6	$2.73 \cdot 10^1$	$7.98 \cdot 10^9$
7	$2.91 \cdot 10^1$	$2.98 \cdot 10^9$
8	$2.99 \cdot 10^1$	$1.07 \cdot 10^9$
9	$2.82 \cdot 10^1$	$3.54 \cdot 10^8$
10	$3.13 \cdot 10^1$	$1.38 \cdot 10^8$
11	$3.04 \cdot 10^1$	$4.68 \cdot 10^7$
12	$3.25 \cdot 10^1$	$1.75 \cdot 10^7$
13	$3.42 \cdot 10^1$	$6.47 \cdot 10^6$
14	$2.63 \cdot 10^1$	$1.74 \cdot 10^6$
15	$3.36 \cdot 10^1$	$7.81 \cdot 10^5$
16	$1.95 \cdot 10^1$	$1.58 \cdot 10^5$
17	$2.23 \cdot 10^1$	$6.36 \cdot 10^4$
18	$1.24 \cdot 10^1$	$1.23 \cdot 10^4$
19	$1.33 \cdot 10^1$	$4.63 \cdot 10^3$
20	$4.50 \cdot 10^1$	$2.90 \cdot 10^1$
21	$3.55 \cdot 10^1$	$8.03 \cdot 10^0$

TABLE A2 Spectrum of relaxation moduli and reference viscosities of process I for PVDF at $T = 55\text{ }^{\circ}\text{C}$.

Mode nr. (-)	Shear modulus G_i (MPa)	Viscosity $\eta_{0,i,\text{ref}}$ (MPa·s)
1	$1.06 \cdot 10^2$	$3.12 \cdot 10^{11}$
2	$2.54 \cdot 10^1$	$1.17 \cdot 10^{10}$
3	$2.34 \cdot 10^1$	$4.25 \cdot 10^9$
4	$1.23 \cdot 10^1$	$8.85 \cdot 10^8$
5	$2.00 \cdot 10^1$	$5.70 \cdot 10^8$
6	$1.13 \cdot 10^1$	$1.27 \cdot 10^8$

TABLE A2 (Continued)

Mode nr. (-)	Shear modulus G_i (MPa)	Viscosity $\eta_{0,i,\text{ref}}$ (MPa·s)
7	$1.54 \cdot 10^1$	$6.87 \cdot 10^7$
8	$1.26 \cdot 10^1$	$2.22 \cdot 10^7$
9	$1.08 \cdot 10^1$	$7.51 \cdot 10^6$
10	$1.25 \cdot 10^1$	$3.46 \cdot 10^6$
11	$1.25 \cdot 10^1$	$1.37 \cdot 10^6$
12	$8.84 \cdot 10^0$	$3.82 \cdot 10^5$
13	$1.23 \cdot 10^1$	$2.09 \cdot 10^5$
14	$1.38 \cdot 10^1$	$9.32 \cdot 10^4$
15	$1.18 \cdot 10^0$	$3.15 \cdot 10^3$
16	$2.60 \cdot 10^1$	$2.75 \cdot 10^4$
17	$1.88 \cdot 10^1$	$3.11 \cdot 10^3$
18	$1.39 \cdot 10^1$	$9.10 \cdot 10^2$

TABLE A3 Spectrum of relaxation moduli and reference viscosities of process I for PVDF at $T = 75\text{ }^{\circ}\text{C}$.

Mode nr. (-)	Shear modulus G_i (MPa)	Viscosity $\eta_{0,i,\text{ref}}$ (MPa·s)
1	$7.51 \cdot 10^1$	$1.71 \cdot 10^{11}$
2	$1.89 \cdot 10^1$	$6.87 \cdot 10^9$
3	$1.26 \cdot 10^1$	$1.82 \cdot 10^9$
4	$1.28 \cdot 10^1$	$7.43 \cdot 10^8$
5	$1.16 \cdot 10^1$	$2.69 \cdot 10^8$
6	$8.03 \cdot 10^0$	$7.44 \cdot 10^7$
7	$1.14 \cdot 10^1$	$4.23 \cdot 10^7$
8	$6.22 \cdot 10^0$	$9.20 \cdot 10^6$
9	$1.00 \cdot 10^1$	$5.92 \cdot 10^6$
10	$6.38 \cdot 10^0$	$1.51 \cdot 10^6$
11	$5.95 \cdot 10^0$	$5.62 \cdot 10^5$
12	$6.64 \cdot 10^0$	$2.51 \cdot 10^5$
13	$7.39 \cdot 10^0$	$1.12 \cdot 10^5$
14	$4.67 \cdot 10^0$	$2.82 \cdot 10^4$
15	$5.62 \cdot 10^0$	$1.36 \cdot 10^4$
16	$8.42 \cdot 10^0$	$8.12 \cdot 10^3$
17	$1.43 \cdot 10^1$	$2.19 \cdot 10^3$
18	$3.09 \cdot 10^0$	$1.90 \cdot 10^2$